HAL open science

Coherent combination of microsecond-pulse tapered amplifiers for a water-vapor differential absorption lidar

Qin Liu, Clément Marque, Sylvie Janicot, Patrick Georges, Gaëlle Lucas-Leclin

To cite this version:

Qin Liu, Clément Marque, Sylvie Janicot, Patrick Georges, Gaëlle Lucas-Leclin. Coherent combination of microsecond-pulse tapered amplifiers for a water-vapor differential absorption lidar. OPTO - Novel In-Plane Semiconductor Lasers XXII, Proc. SPIE 12440, Novel In-Plane Semiconductor Lasers XXII, 12440, pp.124400L, 2023, 10.1117/12.2647246 . hal-04255296

HAL Id: hal-04255296

https://hal-iogs.archives-ouvertes.fr/hal-04255296

Submitted on 23 Oct 2023

HAL is a multi-disciplinary open access archive for the deposit and dissemination of scientific research documents, whether they are published or not. The documents may come from teaching and research institutions in France or abroad, or from public or private research centers.

L'archive ouverte pluridisciplinaire **HAL**, est destinée au dépôt et à la diffusion de documents scientifiques de niveau recherche, publiés ou non, émanant des établissements d'enseignement et de recherche français ou étrangers, des laboratoires publics ou privés.

Distributed under a Creative Commons Attribution - NonCommercial - ShareAlike 4.0 International License

Proc. SPIE 12440, Novel In-Plane Semiconductor Lasers XXII, 124400L (15 March 2023); doi: 10.1117/12.2647246

Coherent combination of microsecond-pulse tapered amplifiers for a water-vapor differential absorption lidar

Qin Liu[a], Clément Marque[a], Sylvie Janicot[a], Patrick Georges[a], Gaëlle Lucas-Leclin*[a]
[a]Université Paris-Saclay, Institut d'Optique Graduate School, CNRS, Laboratoire Charles Fabry, 91127 Palaiseau, France

ABSTRACT

Remote sensing techniques are critical in atmospheric research, such as the monitoring of the low tropospheric temperature and the water vapor distribution. Lidar is one type of remote sensing technique that can deliver an atmospheric measurement with high spatial and temporal resolutions[1]. In this paper, we describe a diode-laser-based laser source at 828 nm in a master oscillator power amplifier (MOPA) architecture designed to be compatible with a water-vapor differential absorption lidar (DIAL). Two tapered amplifiers with a pulse duration of 1 µs and a repetition rate of 10 kHz are injected by a single-frequency DBR seed laser diode and coherently combined. The performance of the seed DBR laser diode and the tapered amplifiers are characterized. The phase dynamics during the pulse are analyzed, and we demonstrate that they do not significantly reduce the combining efficiency. The combined power is stabilized by a hill-climbing algorithm which actively corrects the low-frequency environmental noise. The average combined pulse energy is highly stable with relative fluctuations $\sigma_{on} = 0.4\%$. The combined pulse energy reaches 10.3 µJ at the maximal operation current of 8.1 A with a combining efficiency above 82% ± 5%. This work demonstrates the coherent beam combination of micropulse tapered amplifiers and the interests of these techniques in lidar applications.

Keywords: Coherent beam combination, tapered laser amplifier, lidar, high-brightness diode lasers

1. INTRODUCTION

Atmospheric monitoring is a crucial field of research that requires accurate and high-resolution measurements, and lidar is a key technique in this context. In recent years, diode-laser-based architectures have been demonstrated as a promising architecture for the development of direct-detection compact lidars, with long-term autonomous operation[2,3]. Among them, Differential Absorption Lidars (DIAL) provide a self-calibrated, range-resolved mapping of atmospheric components[2].

They rely on a high spectral purity pulsed laser source, which operates at two wavelengths alternatively—one at the absorption line and the other out of it. Comparison of two retro-diffusion signals gives access to the spatial distribution of the molecule under interest. Ground-based water-vapor DIAL microlidars with transmitted pulse energy > 5 µJ at a ~10 kHz repetition rate have been constructed and successfully validated at NCAR[2]. Still, a further increase in pulse energy would improve the performance of DIAL systems.

Different approaches of superposition of multiple laser beams may increase the overall energy, but only coherent beam combination (CBC) preserves the spectral purity and beam quality of the laser beams[4]. Previous research has demonstrated the feasibility of CBC for diode lasers in continuous-wave (CW) operation, with up to 47 edge-emitting ridge-waveguide amplifiers resulting in a combined power of 40 W at 1064 nm[5]. Additionally, CBC has also been achieved for TSOAs in CW operation[6] and in pulsed regimes with millisecond-long pulses[7].

In this study, we present the first demonstration of CBC of two TSOAs under a microsecond-pulse regime. The approach is based on a master oscillator–power amplifier architecture, where a CW high-spectral purity DBR laser diode is amplified in two pulsed semiconductor amplifiers in parallel. The coherence between the two amplified beams is thus preserved so that they can be coherently superposed on a free-space beam splitter. We investigate the phase dynamics of the TSOAs during the optical pulse. The phase difference between the amplified beams is actively locked to maximize the coherently combined pulse energy. The combining efficiency is thoroughly investigated to understand its limitations. Additionally, we measure the mid-term average power stability of the system. The results of this study suggest that CBC is a promising approach for the development of high peak-power diode-laser-based pulsed sources required in water-vapor differential absorption lidar.

2. SEED SOURCE PERFORMANCE

In our experiment, we use a single-frequency DBR laser diode (Photodigm, Inc., PH828DBR180T8) operating in CW operation at 828 nm. The maximal output power is 235 mW at 300 mA. The laser diode is mounted in a TO-8 package, allowing us to control and monitor the package temperature. The wavelength of the laser diode can be switched between the targeted online wavelength (828.187 nm in vacuum) and offline wavelength (828.287 nm in vacuum)[8] by temperature tuning (ΔT =1.8 °C). The seed beam is collimated and isolated by a dual-stage isolator (< 60 dB) to avoid optical feedback from the tapered amplifiers. It is coupled into a single-mode polarization-maintaining (PM) fiber and connected to a 90:10 PM fiber coupler. The 10% fiber port is used to monitor the seed power and wavelength.

The relative fluctuation of the fiber-coupled seed power is 0.4% over one hour (shown in figure 1(left)), as measured behind a polarizing beam splitter cube. The long-term wavelength stability is measured by a high-precision wavemeter (resolution = 0.01 pm) as shown in figure 1 (right). For 100 min, the wavelength is stable with maximal fluctuations < 0.15 pm which is attributed to slow environmental temperature variations. The wavelength stability fulfills the requirements for the water-vapor lidar application, for the width of the absorption line of interest is 2.1 pm (0.9 GHz)[9].

Commenté [GLL1]: Would we have a power measurement stability to add ?

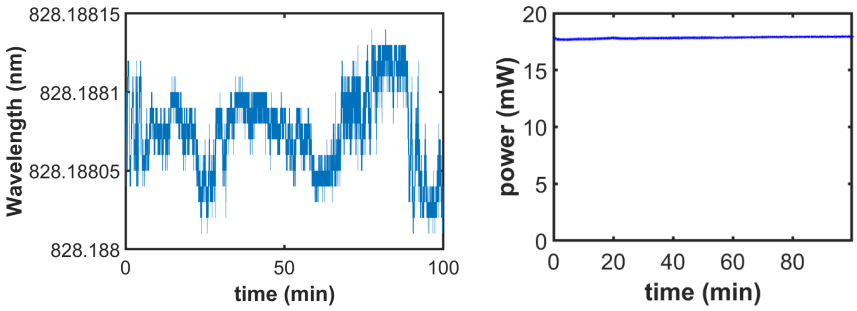

Figure 1. The DBR wavelength variation during 100 min of measurement.

Figure 1. (left) The DBR power stability measured behind a polarizing beam splitter cube at 100 mA. (right) The DBR wavelength variation during 100 min of measurement.

3. AMPLIFIER CHARACTERIZATION

3.1 Standard Characteristics

The power amplifiers are commercial tapered semiconductor optical amplifier (TSOA) devices packaged with a C-mount heatsink (TSOA, Eagleyard Photonics, EYP-TPA-0830) centered at 830 nm. A TSOA consists of a single-mode ridge waveguide and a flared section. Each device is fixed onto a Cu-block which acts both like an anode and an extra heatsink whose temperature is monitored by a thermistor. The maximal operating current under CW operation of the TSOA, according to the manufacturer, is 3 A at which the CW optical power is 1.1 W. In our case, the amplifiers are electrically driven by commercial current drivers (PicoLAS, LDP-V 50-100) with a pulse duration of 1 µs, and a repetition rate of 10 kHz. With a duty cycle of 1%, the amplifiers can be overdriven far above the specification without evidence of thermal rollover. The connection between the current driver and the amplifier electrodes is carefully designed with copper layer tapes to reduce the pulse rise time to 40 ns.

The fiber-coupled seed beam is coupled into the ridge section with an aspheric lens (L_4: F_4 = 8 mm) behind a fiber collimator (L_3: F_3 = 18 mm). On the output side of the TSOAs, the amplified beam is astigmatic because the virtual sources of the beam in the slow and fast axes do not overlap. The fast axis of the beam is collimated by an aspheric lens (L_5: F_5 = 2.75 mm) and the slow axis of the beam is collimated further by a cylindrical lens (L_6: F_6 = 12.7 mm). The amplified beam is linearly polarized and parallel to the junction plane. The beam radius of the astigmatic-corrected beam is recorded around its focus with a CMOS camera and an automatic translation stage. The $M^2_{4\sigma}$ factor is computed from the data with a weighted least-square curve fit. The beam radius propagation data is shown in figure 2 (left). The $M^2_{4\sigma}$ of the amplified

beams is below 4.9 × 1.4 at a drive current I ≤ 5.3 A. The Cu-block and the benches for the coupling optics are glued to an aluminum plate. The aluminum plate and the coherent combining elements are screwed to an aluminum breadboard (see section 4) that is temperature controlled by Peltier elements. The device temperature is fixed at 21°C during its operation.

Commenté [GL2]: It should be useful to add the uncertainties on the M2 measurements ± ??

The amplified peak power characterization P_{out} as a function of the incident seed power P_{in} at a drive current of 5.3 A is shown in figure 2 (right). The output power follows the gain saturation relation

$$P_{out} = G_0(I) \times \frac{P_{in}}{1 + \frac{P_{in}}{P_{sat}}},$$

where $G_0(I)$ is the small signal gain at the drive current I, P_{in} is the injection power and P_{sat} is the saturation power. The saturation powers for both amplifiers are below 4 mW under our operating range (I ≤ 8.1 A). The injection powers P_{in} are therefore chosen to be above 24 mW to ensure saturation of both amplifiers. The maximal peak power reaches 6.7 W per amplifier at 8.1 A with a constant slope efficiency of 1.1 W/A throughout our operating range (see figure 8). A higher peak power could be achieved with a higher drive current, but we did not further overdrive the TSOAs to avoid catastrophic optical damage to the devices.

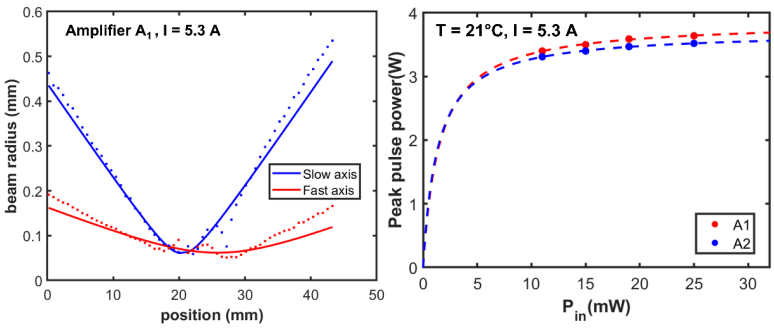

Figure 2. (left) The beam propagation data of amplifier A_1 with $M^2_{4\sigma}$ factor = 4.9 × 1.4 at a drive current 5.3 A. (right) The characteristics of the peak pulse power P_{out} (P_{in}) of amplifiers A_1 and A_2 fitted with the saturation formula at 5.3 A.

3.2 Phase drift analysis during the pulse

During the pulse, the amplifier is in a steady state regarding the carrier dynamics, which is much faster than the pulse duration. Nevertheless the temperature of the active region increases under the thermal load[10]. Therefore, the accumulated phase evolves during the pulse, mostly because of the thermo-optic effect which changes the refractive index. To characterize this phase drift, the phase evolution $\Delta\varphi(t)$ during the pulse was measured in a I/Q architecture, by interfering the amplified beam with the 10% seed source of the fiber coupler as shown in figure 3. The coherent seed output was circularly polarized by a quarter wave plate and then superpose with the linearly polarized amplified beam. The interfered output was separated into an in-phase component ($I(t) \propto \cos\Delta\varphi(t)$) and a quadrature component ($Q(t) \propto \sin\Delta\varphi(t)$) (shown in figure 3) by a polarizing beam splitter[11]. The minimal and maximal interference envelopes $Q_{min}(t)$, $Q_{max}(t)$, $I_{min}(t)$, and $I_{max}(t)$, shown as the dotted lines, were evaluated based on multiple measurements. The piston phase difference $\Delta\varphi(t)$ between the seed and the amplified beam was computed as

$$\Delta\varphi(t) = \arctan\left\{\frac{\left[Q(t) - \left(\frac{Q_{max}(t)+Q_{min}(t)}{2}\right)\right] \Big/ \left[\frac{Q_{max}(t)-Q_{min}(t)}{2}\right]}{\left[I(t) - \left(\frac{I_{max}(t)+I_{min}(t)}{2}\right)\right] \Big/ \left[\frac{I_{max}(t)-I_{min}(t)}{2}\right]}\right\} \quad (1)$$

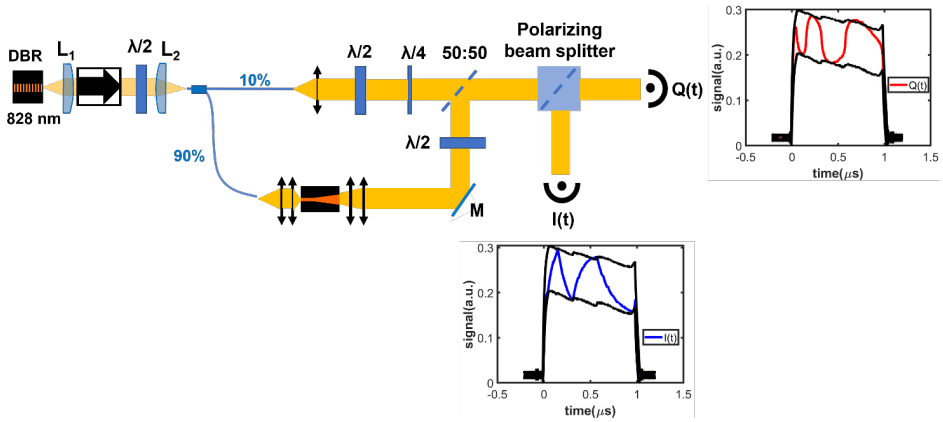

Figure 3. Experimental setup for the phase drift measurement. An example of the interfering power evolution between the circularly polarized seed output and the linearly polarized amplified beam is shown. I(t) and Q(t) are the signals at the two polarization axes after the polarizing beam splitter and the maximal and minimal interference envelopes are plotted in black.

The phase drift during the pulse at 2.2 A, 5.3 A, 6.9 A, and 8.1 A respectively are shown in figure 4 (left). The total phase drift during the $\tau = 1\ \mu s$ increases linearly with the current, and reaches 4.6 π at 8.1 A. It corresponds to a temperature rise of about 2°C. After the first 50 ns of the pulse, the phase varies almost linearly with time, which reflects the linear evolution of the temperature of the active region induced by heat deposal before heat diffusion. The step-like evolution of $\Delta\varphi(t)$ at high current is attributed to the enhancement of resonances within the amplifier as its optical gain increases. The phase drift measured during the first 50 ns of the pulse does not follow the same trend due to the dynamics and possible experimental uncertainties induced by the fast modulation of the amplifier drive current. The consistency of the result is verified by overlapping 20 consecutive phase drift measurements at 8.1 A. The measurement discrepancy or the difference between the maximal and minimal phase drift envelopes during the pulse is 0.11π on average at the highest operating current 8.1 A. Therefore, the linear phase evolution is repeatable from pulse to pulse.

Commenté [GL3]: ? not in Figure 4, the measurement is done at 5.3 A. Do you mean that the phase difference of 0.11 pi is at 8.1 A ? (as in my correction)

The phase drift of two amplifiers, $\varphi_1(t)$ and $\varphi_2(t)$, are compared in figure 4 (right). The phase drift evolutions are similar between the two amplifiers with the maximal phase drift difference of ~ 0.17 π at a drive current 5.3 A. Considering the phase discrepancy, the combined pulse power evolution is computed as

$$P_{CBC}(t) = \frac{1}{2}\left[P_1(t) + P_2(t) + 2\sqrt{P_1(t) \times P_2(t)} \times \cos(\varphi_1(t) - \varphi_2(t))\right] \quad (2)$$

where $P_1(t)$ and $P_2(t)$ are the pulse power profile of amplifier A_1 and A_2 respectively. $P_{CBC}(t)$ is calculated in figure 4 (right) using the experimental time profiles $P_i(t)$ and $\varphi_i(t)$ (i = 1,2) at I = 5.3 A. The combining efficiency, based on the combined energy per pulse, is evaluated by

$$\eta_{CBC}^{(E)} = \frac{\int_0^{1\mu s} P_{CBC}(t)dt}{\int_0^{1\mu s} P_1(t)\,dt + \int_0^{1\mu s} P_2(t)\,dt} \quad (3)$$

Commenté [GL4]: Change the notation here, as the definition is not the same as the one used in section 4.3 ?

The estimated CBC efficiency is $\eta_{CBC}^{(E)}$= 98 % at 5.3 A. Therefore, although the phase drift of individual amplifier is high during the pulse, the evolution of the phase drift is similar between the two amplifiers and the combining efficiency is not significantly affected. The phase drift during the pulse does not need to be corrected for the coherent combination experiment.

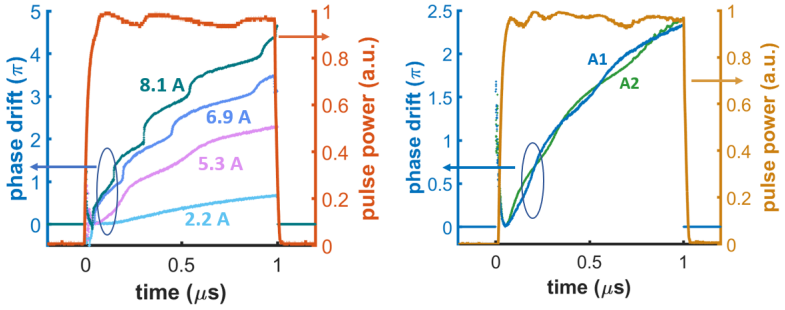

Figure 4. (left) The phase drift during the pulse with the magnitude of 0.7 π, 2.3 π, 3.5 π, 4.6 π respectively at a drive current of 2.2 A, 5.3 A, 6.9 A, and 8.1 A. The pulse power profile (red) is plotted for reference. (right) The phase drift comparison between two amplifiers at 5.3 A. The combined pulse power profile (brown) calculated from Eq. (2) is plotted.

4. EVALUATION OF COHERENT COMBINATION PERFORMANCE

4.1 Experimental setup

The coherent beam combination of semiconductor amplifiers is realized by a master oscillator power amplifier (MOPA) architecture as shown in figure 5 (left). The amplified beams are recombined in a Mach-Zehnder interferometer in free space. The optical path length difference between the arms of amplifiers is actively controlled to maintain the coherent combination. The beams are superposed on a non-polarizing 50:50 beam splitter. The coupling optics, the tapered amplifiers, and the combining elements are mounted on a 22 cm × 18 cm × 0.6 cm aluminum breadboard as shown in figure 5 (right), whose temperature is controlled by Peltier elements.

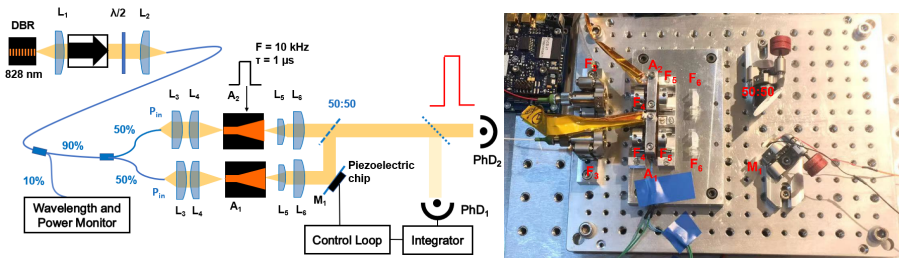

Figure 5. (left) The experimental setup of the laser source. (right) The photo of the setup. The tapered amplifiers, coupling lenses, and beam splitters are mounted on an Al breadboard (22 cm × 18 cm × 0.6 cm) that is thermally controlled by Peltier elements.

4.2 Phase stabilization

The amplifier current drivers are externally triggered by a function generator with a synchronization delay of 10 ns. The phase drifts during the pulse, as discussed in section 3.2, are similar between the two beams and do not reduce the combining efficiency significantly. Therefore, no high-frequency phase correction within the pulse is required. However, phase correction is required to reduce the low-frequency phase fluctuations and maintain the combined power at its maximum. This phase noise is caused by the acoustic and thermal noises of the whole interferometer with a time scale > 1 s and can affect the combined pulse energy stability. The phase is actively controlled by a servo loop which adjusts the optical path length of amplifier A_1, by means of the voltage applied to the piezoelectric transducer (PZT) attached to the folding mirror M_1 whose location defines the optical path length difference between the amplified beams. A small portion of the combined pulse, measured by a photodiode PhD_1, is integrated by an RC circuit (cut-off frequency = 19 Hz) to generate the error signal for the servo loop. A hill-climbing algorithm is designed and coded in a microcontroller whose voltage output controls the deformation of the PZT and the optical path length of A_1. It generates a voltage dither (amplitude $\Delta V \geq 0.06$ V) to the PZT with a step duration of 65 ms; the combined average power before and after the voltage perturbation is measured by PhD_1. A voltage step is then applied to maximize the combined pulse power. The servo-loop correction frequency is 5 Hz. To reduce the extra phase noise introduced by the dithering voltage, a latency period of 260 ms is applied once the maximal power is reached. Since the phase instability is caused by low-frequency thermal and acoustic noises, our servo loop is sufficient to maintain phase matching and combined power stability.

The combined power stability at 6.9 A is illustrated in figure 6. PhD_1 measures the average pulse power $P_{CBC} = E_{CBC} \times F_{rep}$, which is proportional to the average pulse energy E_{CBC}. PhD_2 measures time-resolved pulse profiles. The long-term pulse energy stability is characterized by the average pulse energy measured with PhD_1 (see figure 6 (left)). Even without any phase stabilization, it is noteworthy that the average pulse energy fluctuations are low, , thanks to the robustness of our experimental setup: the relative standard deviation of the combined power is 5.0 % during more than 1000 s of measurement. The stability can be further improved with our servo-loop to 0.4 % at all drive currents, limited by the phase perturbation introduced by the voltage dither. About 500 phase-controlled pulse profiles measured by PhD_2 are overlapped in the density plot shown in figure 6 (right). The mean peak power fluctuation between profiles is 1.2% which is better than the peak power stability without the control (5.0%). The efficiency of phase stabilization in frequency domain is characterized with the relative intensity noise (RIN) power spectral density (PSD) at 6.9 A (figure 7). The phase noise is successfully corrected at frequency $f < 0.5$ Hz. The servo-loop introduces some extra noise at frequency $f > 2$ Hz with one of the peaks at 5 Hz corresponding to our correction frequency. However, the magnitudes of these noise are significantly lower than the low-frequency phase noise and therefore, the servo-loop successfully maximize the combined power. Phase stability can be improved with a heterodyne detection of high-frequency phase modulation and a PID regulator to stabilize the combined power. With this technique, our combined power stability will not be limited by the modulation amplitude.

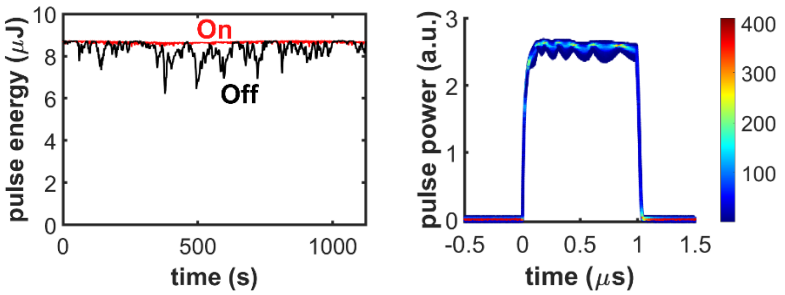

Figure 6. (left) The averaged combined pulse energy for more than 1000 s measured with and without the phase control at 6.9 A. (right) 500 sets of phase-controlled combined pulse profiles at 6.9 A in a density plot.

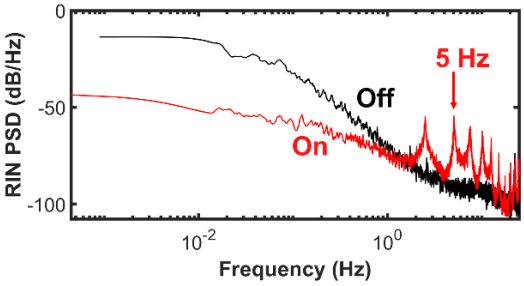

Figure 7. The relative intensity noise (RIN) power spectral density (PSD) of the averaged combined pulse energy with and without the phase control.

4.3 Combining efficiency evaluation

The peak pulse power of the combined pulse and the individual amplifier pulse outputs were measured from 2.2 A to 8.1 A as shown in figure 8, based on the measurement of the average power $P_{ave} = P_{peak} \times dc$ with the duty cycle dc = 1% under our experimental conditions. The drive current of amplifier A_2 was slightly adjusted by ± 5% to maintain the phase drift matching during the pulse. The maximal combined peak power reaches 10.3 W at 8.1 A with each amplifier contributing 6.7 W. The combining efficiency is experimentally evaluated with different methods, based on either the average power ($\eta_{CBC}^{(avg)}$), the peak pulse power ($\eta_{CBC}^{(pk)}$), and the pulse energy from the integrated pulse profile ($\eta_{CBC}^{(E)}$):

- The average-power combining efficiency is $\eta_{CBC}^{(avg)} = P_{CBC}^{(avg)}/(P_1^{(avg)} + P_2^{(avg)})$ where $P_{CBC}^{(avg)}$, $P_1^{(avg)}$, and $P_2^{(avg)}$ are respectively the average powers of the combined beam and the individual amplified beams measured by a thermal power-meter.

- The peak-pulse-power combining efficiency ($\eta_{CBC}^{(pk)}$) is evaluated based on the peak pulse power measured by a fast photodiode. A triangular voltage ramp of a corresponding phase change of 3π is applied to the piezoelectric transducer (PZT) attached to the combining mirror M_1. A hundred pulse profiles are recorded and overlapped (shown in figure 9 (left)). The mean peak power during the central 800 ns of the pulse is computed for each pulse profile. The pulse profiles with the maximal and minimal mean peak power are selected (red and blue pulse profiles in figure 9 (left)) and their mean peak power $P_{max}^{(pk)}$ and $P_{min}^{(pk)}$ (dotted line in figure 9 (left)) are recorded. The peak-pulse-power combining efficiency is $\eta_{CBC}^{(pk)} = P_{max}^{(pk)}/(P_{max}^{(pk)} + P_{min}^{(pk)})$.

- The combining efficiency $\eta_{CBC}^{(E)}$ is evaluated based on the integrated pulse profile. With the same voltage ramp, a hundred pulse profiles are recorded and the pulse energy $E = \int_0^{1\mu s} P(t)dt$ is computed for each profile (figure 9 (right)). The profiles with the maximal and minimal pulse energy E_{max} and E_{min} are selected. The combining efficiency is $\eta_{CBC}^{(E)} = E_{max}/(E_{max} + E_{min})$.

In the last two methods, the minimum and maximum measurements correspond to, respectively, in-phase ($\Delta\varphi$=0) and out-of-phase (($\Delta\varphi = \pi$) interferences. From equation (2), it is straightforward to check that $P_{max} + P_{min} = P_1 + P_2$, assuming that there are no optical loss on the 50:50 beam-splitter.

The combining efficiencies evaluated with those different methods at each drive current are shown in figure 8. The average efficiency decreases from 88% ± 4% at 2.2 A to 82% ± 5% at 8.1 A with uncertainties estimated from the difference between evaluation methods.

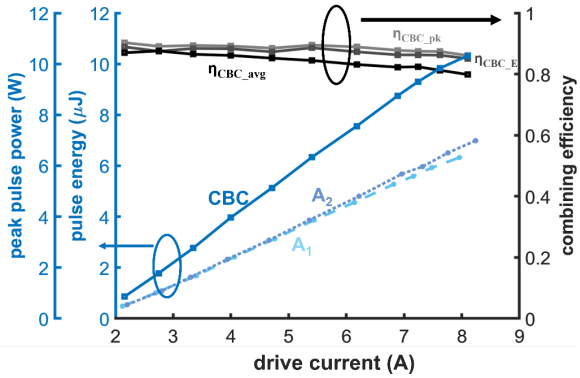

Figure 8. The peak pulse power of the combined pulse and the individual amplified pulses and the corresponding combining efficiency evaluated based on different methods from 2.2 A to 8.1 A.

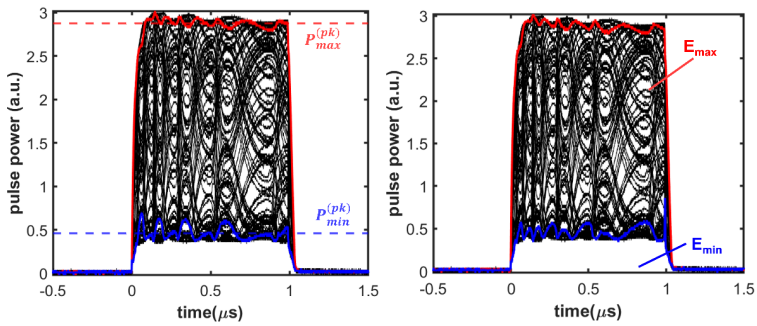

Figure 9. (left) The 100 sets of overlapped pulse profiles recorded while the piston phase difference is ramped. The pulse profile with the maximal and minimal mean peak power during the 800 ns of the pulse are highlighted and their mean peak power level $P_{max}^{(pk)}$ and $P_{min}^{(pk)}$ are labeled. (right) With the same 100 sets of overlapped pulse profiles, the pulse profile with the maximal and minimal integrated pulse energy are highlighted and their pulse energy E_{max} and E_{min} are labelled.

The combining efficiency is compared with the theoretically evaluated combining efficiency based on the spatial overlap of the amplified beam profile $I_1(x,y)$ and $I_2(x,y)$ recorded with a CMOS camera positioned 40 cm behind the beam splitter in the combined beam. The theoretical local combining efficiency is

$$\eta_{local}(x,y) = \frac{1}{2}\frac{\left|\sqrt{I_1(x,y)}e^{i\varphi_1(x,y)} + \sqrt{I_2(x,y)}e^{i\varphi_2(x,y)}\right|^2}{\left|\sqrt{I_1(x,y)}e^{i\varphi_1(x,y)}\right|^2 + \left|\sqrt{I_2(x,y)}e^{i\varphi_2(x,y)}\right|^2} \quad (4)$$

where $\varphi_1(x,y)$ and $\varphi_2(x,y)$ are the phase profiles of the amplified beams. The total combining efficiency is computed from an intensity-weighted average of the local combining efficiency[12]

$$\eta_{CBC}^{spatial} = \frac{\iint[(I_1(x,y) + I_2(x,y)) \times \eta_{local}(x,y)]dxdy}{\iint[I_1(x,y) + I_2(x,y)]dxdy} \quad (5)$$

Commenté [GL5]: Add reference to Goodno – either Optics Express or in the CBC book

Due to the existence of side lobes in the intensity profiles, the phase profiles of the amplified beams $\varphi_n(x,y)$ cannot be correctly measured with a wavefront sensor. Therefore, the phase profiles in our evaluation are assumed to be overlapped perfectly. The beam profiles $I_n(x,y)$ of amplifier A_1 and A_2 and the local combining efficiency at 8.1 A are shown in figure 10. The theoretical spatial combining efficiency $\eta_{CBC}^{spatial}$ is estimated to 94%, and is constant throughout our range of operation. It is worth noticing that the beam profiles are recorded with an integration time of 40 ms so that the theoretical combining efficiency is an average combining efficiency over several hundred of pulses. The combining efficiency including the piston phase mismatch between two amplified beams (see section 3.2) is therefore ~ 92%.

The combining efficiencies achieved experimentally are lower than the theoretically evaluated results which could be caused by the slight difference between beam collimations and polarization. Still, these values are comparable to previous results achieved with different operation conditions[6,7,13]. Thus we did not overdrive the amplifiers above 8.1 A to avoid further reduction in combining efficiencies and possible catastrophic optical damage.

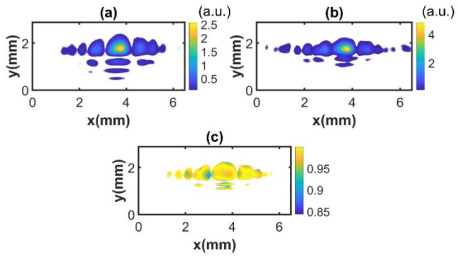

Figure 10. The beam spatial profiles of amplifier A_1 (a) and A_2 (b) and the local combining efficiency $\eta_{local}(x,y)$ (c) computed based on the spatial overlap of the amplifier beams at 8.1 A.

5. CONCLUSION

We demonstrated the coherent combination of two tapered amplifiers in MOPA configuration. The tapered amplifiers are pulse-pumped with pulse duration of 1 µs and repetition rate of 10 kHz and they are injected by a single-frequency DBR laser diode. The phase dynamics of the tapered amplifiers are analyzed. The coherently combined beam is linearly polarized, reaching a pulse energy of 10.3 µJ (10.3 W) with a combining efficiency of 82% ± 5%. The beam quality of the combined beam remains comparable to the individual amplifiers'one, with $M^2_{4\sigma} \leqslant 4.7 \times 1.3$ at all operating currents. The combined pulse energy is stabilized by a hill-climbing algorithm with stability of 0.4 %. The spectral purity of the amplified beam is assume to preserve the linewidth of the seed laser since the amplifiers and the coherent beam combination technique is not supposed to deteriorate the spectral linewidth. This performance has demonstrated the application of coherent combination of semiconductor amplifiers in water vapor differential absorption lidar. Further increase of pulse energy can be achieved by coherently combining more amplifiers.

REFERENCES

[1] Wandinger, U., "Introduction to Lidar," in *LIDAR: range-resolved optical remote sensing of the atmosphere*, Weitkamp., C., eds. (Springer, 2005), pp. 1–18.

[2] Spuler, S. M., Repasky, K. S., Morley, B., Moen, D., Hayman, M. and Nehrir, A.R., "Field-deployable diode-laser-based differential absorption lidar (DIAL) for profiling water vapor," Atmos. Meas. Tech., 8, 1073–1087 (2015).

[3] Spuler, S. M., Hayman, M., Stillwell, R. A., Carnes, J., Bernatsky, T. and Repasky, K. S., "MicroPulse DIAL (MPD) – a diode-laser-based lidar architecture for quantitative atmospheric profiling," Atmos. Meas. Tech., 14, 4593–4616 (2021).

[4] Fan, T. Y., "Laser beam combining for high-power, high-radiance sources," IEEE J. Sel. Top. Quantum Electron., 11, 567–577 (2005).

[5] Creedon, K. J., Redmond, S. M., Smith, G. M., Missaggia, L. J., Connors, M. K., Kansky, J. E., Fan, T. Y., Turner, G. W. and Sanchez-Rubio, A., "High efficiency coherent beam combining of semiconductor optical amplifiers," Opt. Lett. 37, 5006–5008 (2012).
[6] Albrodt, P., Jamal, M. T., Hansen, A. K., Jensen, O. B., Blume, G., Paschke, K., Crump, P., Georges, P. and Lucas-Leclin, G., "Coherent combining of high brightness tapered amplifiers for efficient non-linear conversion," Opt. Express 27, 928–937 (2019).
[7] Albrodt, P., Niemeyer, M., Crump, P., Hamperl, J., Moron, F., Georges, P. and Lucas-Leclin, G., "Coherent beam combining of high power quasi continuous wave tapered amplifiers," Opt. Express 27, 27891–27901 (2019).
[8] Nehrir, A. R., "Development of an eye-safe diode-laser-based micro-pulse differential absorption lidar (MP-DIAL) for atmospheric water vapor and aerosol studies", Ph.D. thesis, Montana State University, 2011.
[9] Repasky, K. S., Moen, D., Spuler. S. M., Nehrir, A. R. and Carlsten, J. L., "Progress towards an autonomous field deployable diode-laser-based differential absorption lidar (DIAL) for profiling water vapor in the lower troposphere," Remote Sens. 5, 6241-6259 (2013).
[10] Coldren, L. A., Corzine, S. W. and Mašanović, M. L., [Diode Lasers and Photonic Integrated Circuits], John Wiley & Sons, Inc., New Jersey (2012).
[11] Huang, R. K., Chann, B., Missaggia, L. J., Augst, S. J., Connors, M. K., Turner, G. W., Sanchez-Rubio, A., Donnelly, J. P., Hostetler, J. L., Miester, C. and Dorsch, F., "Coherent combination of slab-coupled optical waveguide lasers," Proc. SPIE 7230, 72301G (2009).
[12] Goodno, G. D. and Rothenberg, J. E., "Engineering of coherently combined, high-power laser systems," in *Coherent Laser Beam Combining*, Brignon, A., ed. (Wiley-VCH, Weinheim, Germany, 2013), p. 3–44.
[13] Lucas-Leclin, G., Albrodt, P., Pabœuf, D., Schimmel, G., and Georges, P., "Coherent beam combining architectures for high-power laser diodes," in *Advances in High-Power Fiber and Diode Laser Engineering*, I. Divliansky, eds. (The Institution of Engineering and Technology, London, United Kingdom, 2019), pp. 37–87.